

Emission characteristics of the projectile fragments at relativistic energy

M K Singh¹, A K Soma², R Pathak¹ and V Singh^{2*}

¹Department of Physics, Tilakdhari Postgraduate College, Jaunpur 222 002, UP, India

²Nuclear and Astroparticle Physics Lab, Department of Physics, Banaras Hindu University, Varanasi 221 005, UP, India

Received: 25 July 2011 / Accepted: 28 June 2012 / Published online: 28 July 2012

Abstract: A projectile ($^{84}\text{Kr}_{36}$) having kinetic energy around 1 A GeV has been used to expose NIKFI BR-2 emulsion target at GSI, Darmstadt, Germany. A total of 700 inelastic events has been identified and used in the present studies on projectile fragments. The emission angle of the projectile fragments are strongly affected by charge of the other projectile fragments emitted at same time with different emission angle is observed. The angular distribution studies show symmetrical nature for lighter charge projectile fragments. The symmetrical nature decreased with the charge of projectile fragments. We have observed at $\sim 4^\circ$ of emission angle for double charge projectile fragments, the momentum transfer during interaction is similar for various target species of emulsion. We have also observed a small but significant amplitude peaks on both side of the big peak for almost all light charge projectile fragments having different delta angle values. It reflects that there are a few percent of projectile fragments that are coming from the decay of heavy projectile fragments or any other process.

Keywords: Projectile fragmentation; Nuclear emulsion detector; Heavy fragment decay

PACS Nos.: 25.70.Mn; 14.60.Lm; 25.70.Pq

1. Introduction

Nuclear emulsion detector is one of the oldest detector technologies and has been in use from the birth of experimental nuclear and astroparticle physics. Fortunately, it is a unique and simple detector due to very high position resolution ($\sim 1 \mu\text{m}$) with several other unique features. Nuclear emulsion detector posse's 4π detection capability with hit density of 300–500 grains per mm, compactness of size and large range of ionization sensitivity depends upon nature and need of the experiment. The high resolution allows easy detection of short-lived particles like τ lepton, charmed mesons, etc. The 4π visualization of formed tracks during interaction impelled us to pursue studies on physics beyond the standard model.

2. Experimental configuration

Nuclear emulsion detector composes of silver halide crystals immersed in a gelatin matrix [1, 2] consisting

mostly of hydrogen, carbon, nitrogen, oxygen, silver and bromine while a small percentage of sulfur and iodine are also present. In this experiment, we have employed a stack of high sensitive NIKFI BR-2 nuclear emulsion pellicles of dimensions $9.8 \times 9.8 \times 0.06 \text{ cm}^3$, exposed horizontally to $^{84}\text{Kr}_{36}$ ion at a kinetic energy of around 1 GeV per nucleon. The exposure has been performed at Gesellschaft fur Schwerionenforschung (GSI) Darmstadt, Germany.

Interactions were identified by along-the-track scanning technique [3] using an oil immersion objective of $100\times$ magnification. The beam tracks were picked up at a distance of 5 mm from the edge of the plate and carefully followed until they either interacted with emulsion nuclei or escaped from any surface of emulsion. These events have been examined and analyzed with the help of an OLUMPUS, binocular optical microscope, having total magnification of 2,250X and measuring accuracy better than $1 \mu\text{m}$.

A total of 700 inelastic events produced in ^{84}Kr -emulsion interactions have been located. During event scanning, we have picked up all genuine events in accordance with event selection criteria mentioned in Refs. [4–7]. The interaction mean free path (λ) of ^{84}Kr in nuclear emulsion

*Corresponding author, E-mail: venkaz@yahoo.com

has been determined and found to be 7.50 ± 0.28 cm, which is consistent with the measurements of $\lambda = 7.10 \pm 0.14$ cm reported by DGKLM TV Collaboration [8, 9]. In the present analysis, out of 700 there are 570 events having fulfilled the required criteria [4] for further investigation.

The mean number of fully developed and well separated grains per unit length is called the grain density (g). It is a measure of rate of energy loss. The grain density of a singly charged particle passing in same emulsion at extreme relativistic velocity is called the minimum grain density (g_{\min}). In this experiment, $g_{\min} = 28 \pm 1$ grains per 100 μm . The grain density of a track corresponds to a particular ionization but its actual value depends on the degree of development of emulsion and type of emulsion employed. It is therefore, necessary to introduce another quantity called normalized grain density, defined as $g^* = g/g_{\min}$, where g is observed grain density. All charged secondaries produced in an interaction are classified in accordance with their ionization, range and velocity into the following categories:

- (a) Shower tracks (N_s): Charged particles with $g^* < 1.4$ and relative velocity (β) > 0.7 , and for proton it means energy of $E_p > 400$ MeV. They are mostly fast pions with a small admixture of Kaons and released protons from the projectile which have undergone an interaction. These conditions ensure that showers are filtered from the fragments and knockout protons of the target.
- (b) Grey tracks (N_g): Particles having ionization in the interval $1.4 < g^* < 6.0$ and range $L > 3$ mm are defined as greys. These particles have relative velocity (β) in between 0.3 and 0.7. They are generally knocked out protons of targets having energy $30 < E_p < 400$ MeV but are also admixture of deuterons, tritons and some slow mesons.
- (c) Black tracks (N_b): Particles with range $L < 3$ mm from interaction vertex, $g^* > 6.0$, $\beta < 0.3$ and proton with energy $E_p < 30$ MeV are black tracks. Most of these are produced owing to evaporation of residual target nucleus. The heavily ionizing charged particles ($N_h = N_g + N_b$) are parts of the target nucleus and are also called target fragments.
- (d) Projectile fragments (N_f): These are spectator parts of projectile nucleus with charge $Z \geq 1$ and having velocity close to projectile velocity. The ionization of projectile fragments (PF's) is nearly constant over a few mm of range and emitted within a highly collimated forward narrow cone of $\pm 10^\circ$ whose size depends upon the available beam energy. The forward angle is the angle whose tangent is the ratio of average transverse momentums (p_T) of projectile

fragments to longitudinal momentum (p_L) of the beam. Taking p_L as beam momentum, i.e., Angle (F) = $\tan^{-1}(p_T/p_L) = \sim 9^\circ$ in this experiment. The PF's are further classified into three categories as follows:

- (i) Heavy projectile fragments (N_f): PF's with charge $Z \geq 3$.
- (ii) Alpha projectile fragments (N_α): PF's with charge $Z = 2$.
- (iii) Singly charged relativistic projectile fragments ($N_{Z=1}$): PF's with charge $Z = 1$.

Since, these PF's have velocities nearly equal to initial beam velocity, their specific ionization may be used directly to estimate their charge. Further experimental details have been reported [8, 9].

2.1. Charge estimation of projectile fragments

When any charged particle passes through the medium, it transfers partial or total energy to atoms or molecules of the medium due to interactions or scattering. If transferred energy is large enough to make the outer most orbital electron free, hence ionizes the medium and forms charge particle tracks inside the nuclear emulsion detector. The rate of ionization varies as square of the charge and Inverse Square of ionizing particle velocity according with the Bethe-Block's formula [10]. Ionization measurements are of great help in estimating the charge of projectile fragments. When ionization is low, the certainty in such estimation may be large because as the grain density increases, the adjacent grain becomes unresolved even under a high magnification microscope that increases the uncertainty in charge estimation. In case of higher charge tracks, the grains get clogged to each other to form blobs and it is not possible to count individual grains. Therefore, to estimate the complete range (36 charge unit in present case) of projectile fragments charge various methods has been devised such as grain density, blob and hole density or gap length coefficient, mean gap length, delta rays counting, relative track width measurement for higher charge fragments, and residual range method.

In our experiment, we have used $^{84}\text{Kr}_{36}$ nuclei as a projectile having energy 1 GeV per nucleon. Projectile kinetic energy (84 GeV) is above the relativistic energy criteria. The charge of projectile is 36 units and in case of peripheral and quasi central collisions there are chances for the estimated total charge (Q , sum of all projectile fragments charges) of interaction/event is more than 36 units due to neutron conversion into proton and minimum up to 1 unit of charge.

A single method can not be applied to estimate charges over the entire range as every method has its own limitations [11, 12]. We have adopted the grain density method

for estimation of charge of projectile fragments having charge $Z \leq 4$. The gap length coefficient method is the most accurate methods for determining charge from 5 to 9 and from 10 to 19 estimated by the delta (δ) rays density measurement. Delta rays are the recoil electrons having kinetic energy more than 5 keV and acquire delta shape (δ) with inclination opposite to the beam direction. The fragments having charge in between 19 and 30 have been estimated by relative track width measurements [1] and residual range method is applicable for fragments having charge above 30. The projectile fragments charge spectra presented in this analysis are up to 10 unit charge and employed methods are described below.

2.2. Blob density

A blob is defined as single structure or set of grains clogging to each other. The gap between two adjacent blobs is called hole. The number of blobs (holes) per $100 \mu\text{m}$ is called blob (hole) density and represented by $B(H)$. If the ionization is small, blob density is a good parameter [8, 9, 11–13] to resolve charges but in case of particles with heavy charge, blob density increases up to $Z = 2$ and then drops as blobs continue to coalesce into larger blobs as shown in Fig. 1. Thus, for very large ionization, blob density method is not sensitive.

We have first measured B and H for projectile fragments which are clearly having charge $Z = 1, 2, 3$ and 4 . The measurements plotted as functions of Z^2 are shown in Fig. 1a and b respectively. Therefore, B and H measurements alone can not determine charge over entire range of ionization. The nature of Fig. 1a is well described by Landau distribution with peak at 5.71 ± 0.21 and sigma of

3.30 ± 0.18 where that of Fig. 1b is described by exponential function with slope -6.32 ± 0.28 and constant 3.27 ± 0.03 .

2.3. Gap-length coefficient method

The distance between two successive blobs is defined as gap length. This length is related to ionization caused by the charged particle [11–13]. The ratio of total number of observed gaps to the number of gaps greater than a certain optimum value or the negative slope (G) of the log of frequency distribution of gap length is a measure of grain density and is called Gap Length Coefficient (G). G is proportional to rate of the energy lose of ionizing particle and is obtained by using Fowler–Perkins [2] relation:

$$G = -(1/L)\ln(B/H), \quad (1)$$

where L is the suitable minimum chosen distance between inside edges of developed grains bordering the gap and H is the number of gaps greater than a certain optimum value L normalized to unity.

For considerably low ionization, one may also determine gap-length coefficient from blob density alone by following the relation:

$$B = G \exp(-\alpha G). \quad (2)$$

Here α is the mean diameter of a developed grain [3]. For projectile fragments whose charge could be estimated with this method with ± 1 charge unit certainty to be up to $Z = 8$. We have computed G and plotted it as a function of Z^2 in Fig. 2. The shape of the curve is similar to the earlier reported curves [14].

According to Fowler [15], the optimum value of L occurs when $GL \sim 2.0$, for all values of G . The accuracy

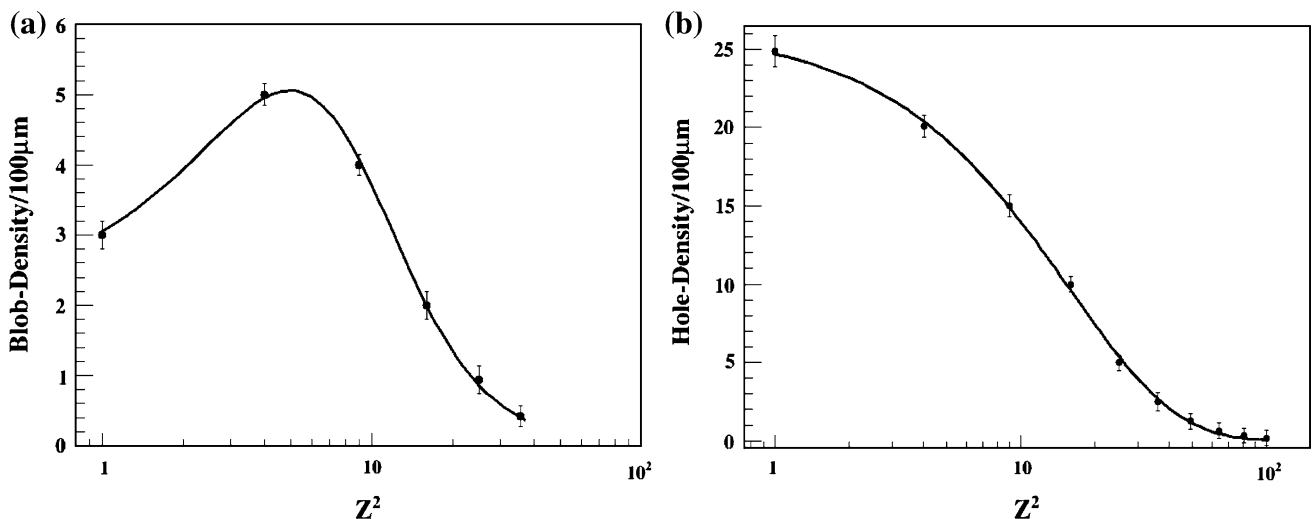


Fig. 1 Calibration curve of **a** Blob's density and **b** Hole's density as a function of square of the projectile fragment's charge (Z^2). Error bar shown on the data points are pure statistical

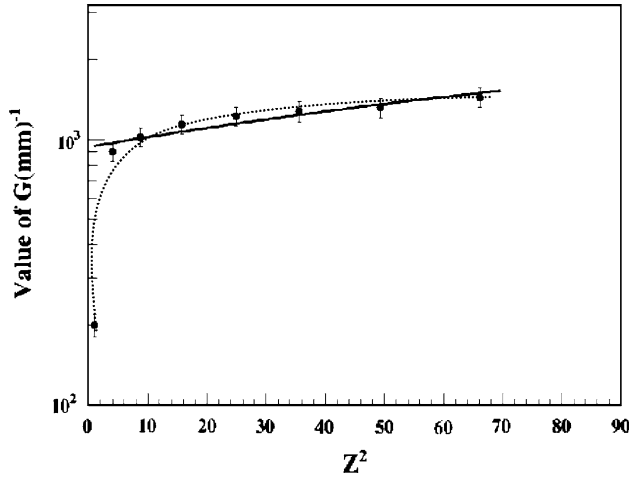


Fig. 2 Calibration curve in terms of gap-length Coefficient as a function of square of the projectile fragment's charge (Z^2). The fitting function is first polynomial with slope 8.46 ± 1.79 and intersection at 936.13 ± 53.05

does not vary appreciably in the interval $1.5 < GL < 2.5$. The statistical error in G can be expressed as

$$dG / G = 1 / [(N_H) \ln(B/H)]^{1/2}. \quad (3)$$

where N_H is number of gaps greater than the length L and H is number of gaps greater than a certain optimum value L , normalized to unit length. We have obtained optimal value of L as $0.98 \mu\text{m}$ which is same as mentioned in Refs. [11, 12]. Minimizing in error is done by setting

$$d/dH [H \log (B/H)]^{1/2} = 0. \quad (4)$$

Solving the differential equation one find that

$$\ln(B/H) = 2.0 \text{ or } B/H = 7.4. \quad (5)$$

The estimation of error is quite reliable as long as $(B/H) > 4$ and $N_B > 4N_H$.

The measurement of gap length coefficient was done for around 600 fragments tracks. We have taken into account all the gaps greater than one division of microscope scale fitted in the eyepiece. The calibrated value of 1 division is equal to $0.98 \mu\text{m}$. However, we do not find any significant change in our final results by varying the value of L , since the measurement for each track is based on counting large number of blobs and gaps and the selection criteria for charge measurement is responsible for different values of B and H .

2.4. Delta ray density method

In a sensitive emulsion, a particle moving at relativistic velocity shows narrow, dense central core around the trajectory of primary particle and number of delta rays which become more and numerous with charge of primary

particle. This method is suitable for particles (fragments) with $Z \geq 10$, the tracks of which virtually have no gaps, comprises in measuring number and/or track lengths of δ shaped electrons produced by charged particle as it ionizes substance along its track. This method is based on the fact that energy and range distributions of delta electrons are dependent on charge (Z) of ionizing particle [16]:

$$\left(\frac{d^2N}{dTdx} \right) = \left[\left(\frac{1}{2} \right) (4\pi N_A r_e^2 m_e c^2) \cdot Z^2 (z/A) (1/\beta^2) \right] \left(\frac{F}{T^2} \right), \quad (6)$$

where T is kinetic energy of delta electrons, x is thickness of the substance passed by ionizing particle, A is atomic weight of atoms in the substance, z is charge of atoms in the substances, $\beta = (v/c)$, v is velocity of ionizing particle, c is velocity of light, N_A is Avogadro's number, F is parameter dependent on spin of ionizing particle at relativistic velocities, it is considered to be constant, m_e is mass of electron and r_e is classical radius of electron. The second term on right hand side is equal to $0.3071 \text{ MeV cm}^2 \text{ g}^{-1}$ [16].

The number of delta rays having kinetic energy more than 5 keV, which escaped from parent particle, may produce recognizable delta shape (δ) tracks with three or more grains inclined against the direction of parent particle, in this measurement. The delta rays having above criteria will contribute to the value of the delta ray density. According to Refs. [16–18], at relativistic velocity, the maximum value of energy of knock-off electrons becomes large compared to any measured minimum delta ray's energy. So, the number of delta rays exceeding a particular minimum energy (W_{\min}) will becomes N_δ , which is

$$N_\delta \sim (2\pi r_0^2) \left[\frac{(m_e c^2)}{W_{\min}} \right] Z^2. \quad (7)$$

Here m_e and c is mass of electron and velocity of light in vacuum, respectively. Generally, we choose a fixed value of W_{\min} for an experiment. In the above equation right hand side is constant except Z . Therefore, the delta ray density (N_δ) is proportional to the square of particle's charge (Z^2).

Development of the method for determining particle charge in detector requires a calibration curve. It has to be based on measured characteristics of tracks produced by particles with known charges. Figure 3 depicts delta ray density for known particle's charges with the best fit line yields a slope of 0.13 ± 0.01 . We can also evaluate empirically, the constant for particular counting convention for the particle of known charges.

By using above mention methods, we know the charge of some of the cross checked fragments. So, we can easily calculate the number of the delta ray density of those charges and we can use those charges for calibration. The charge of other relativistic charged particles can be

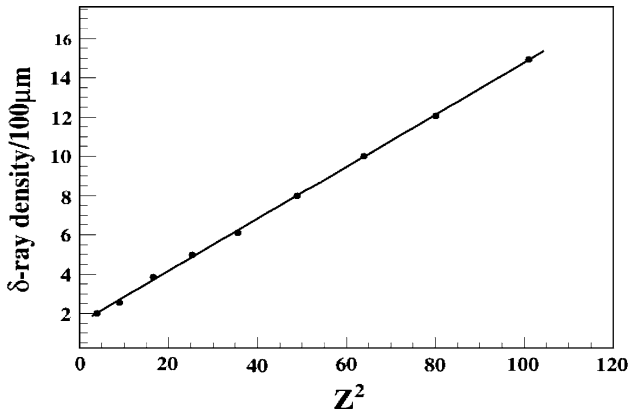


Fig. 3 Calibration curve for the heavy ($9 < Z < 20$) projectile fragment's charge estimation in terms of delta ray density as a function of Z^2

estimated with good accuracy. During scanning we located several electromagnetic dissociated events and we used the projectile fragments of those events to get delta ray density of known charge.

According to Tidmen et al. [20], grain configurations to be counted as delta rays, must attain a minimum displacement of $1.5 \mu\text{m}$ from core of track projected on plane of the emulsion. Dependence of delta ray density on particle charge up to 10 charge units is shown in Fig. 3. For nuclei having charge (Z) >19 , the number of delta rays becomes very large and it is difficult to count their number reliably.

Thus, by using this method, we can measure the charge of the projectile fragments in the range $9 < Z < 20$ and

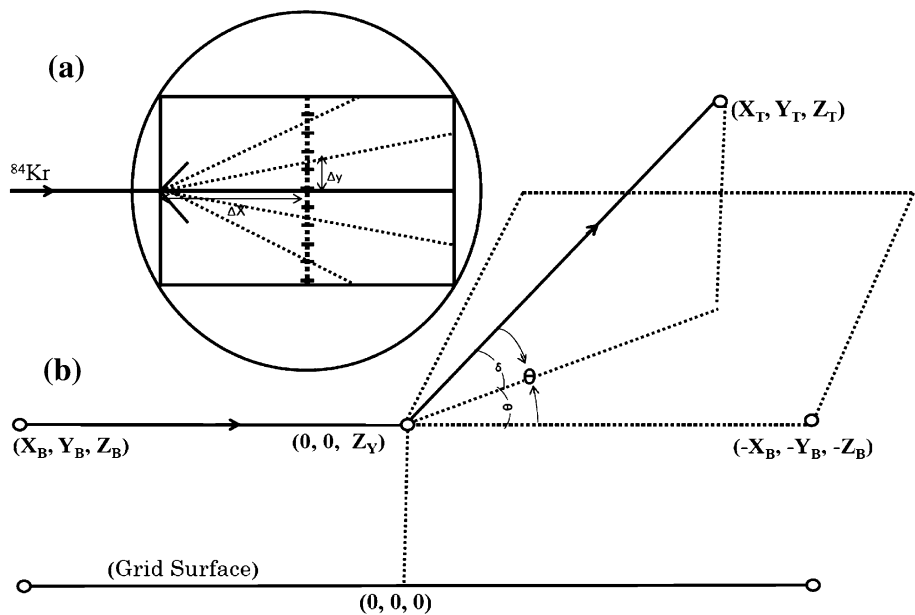
cross check the identity of lower charge projectile fragments estimated by other methods.

2.5. Angle measurement of projectile fragments

The angle measurements of PF's were performed in the narrow forward cone ($\theta_{\text{Lab}} \leq 10^\circ$) [11, 12, 19]. Before starting angle measurement of PF's, the micrometer scale inside the eyepiece is aligned along x -coordinate. When micrometer scale becomes aligned with the help of grains, we align incident the beam tracks along x -coordinate by rotating mechanical stage gently. When beam track and micrometer scale become aligned, the interaction vertex is focused at center of the field of view (at the center of the cross wire fitted in one of the eye piece) of micrometer scale so that the coordinates of interaction vertex are recorded as $x = 0, y = 0$ and $z = z_Y$ (initial z -value i.e. at focused interaction vertex). Then we have shifted the interaction vertex to one end of the x -scale through certain known distance as shown in Fig. 4. The two coordinates (x_T and y_T) of the segment of the PF are read from counter display of digitizing encoder and the third coordinate (z_T) has been accurately recorded.

The spatial configuration of each event was reconstructed by measuring three set of $x, y,$ and z coordinates separated by at least $50 \mu\text{m}$ along $\pm x$ -direction for incident beam track and for each PF's. In other words, coordinate method was used and three point measurement on beam tracks as well as PF's that help us in fitting straight line on PF's and the beam track. Then, we have obtained projected angle of the secondary track (θ_p) in $x - y$ plane (i.e. plane of emulsion) [11, 12]:

Fig. 4 a Procedure of the angle measurement and **b** definition of coordinates, plans and angles



$$\theta_p = \tan^{-1}(\Delta y / \Delta x). \quad (8)$$

The dip angle (θ_d) is given by

$$\theta_d = \tan^{-1} \left[(\Delta z \times S) / (\Delta x^2 + \Delta y^2)^{1/2} \right], \quad (9)$$

where, Δz is change in z -coordinate while travel distance Δx and Δy in the $(x - y)$ plane. S is shrinkage factor. The space angle (θ_s) is given by

$$\theta_s = \cos^{-1} \left[\cos \theta_p / \{1 + \tan^2(\theta_d)\}^{1/2} \right]. \quad (10)$$

The angle of other type of secondary particle tracks has been measured by a Goniometer attached to the eyepiece tube of microscope. The goniometer is provided with a vernier scale that can yield angles with an accuracy of 0.25° .

3. Results and discussion

3.1. $^{84}\text{Kr}_{36}$ projectile fragments charge spectrum up to 10 charge unit

In this analysis, we have adopted some of the above mentioned methods for charge estimation of projectile fragments up to 10 charge units. ^{84}Kr projectile fragments spectrum was compared with other heavier and lighter projectiles fragments charge spectrum having similar beam energy as shown in Fig. 5a and charge spectrum of similar projectile (^{84}Kr) having variable beam energy as shown in Fig. 5b. In both Figures, spectra are presented up to 10 charge units and after that we clubbed all other heavier fragments and called it as more than 10 charge units. The data points are from the present analysis result of $^{84}\text{Kr}_{36}$ at around 1 A GeV and histograms are the results from other experiments. The cross checks of charge estimated with other methods reveals that the obtained charge spectrum has reached accuracy up to ± 1 charge unit. Error bar shown in Fig. 5a and b are the statistical errors.

It is evident from Fig. 5a that the production of single, double and more than 10 charge unit projectile fragments have dependence on projectile mass number. Whereas other charge projectile fragments production shows mixed nature. The minimum and maximum production ranges of projectile fragments for the projectile mass number ranging in between 40 and 238 are as follows: 40–65 % ($Z = 1$); 7 to ~ 18 % ($Z = 2$); ~ 3 –7 % ($Z = 3$); >1 –4 % ($Z = 4$); 0.8–3 % ($Z = 5$); 0.4 to ~ 0.9 % ($Z = 6$); 0.3–0.9 % ($Z = 7$); >0.2 –0.8 % ($Z = 8$); >0.1 –0.5 % ($Z = 9$); >0.1 –0.3 % ($Z = 10$) and 4 to ~ 10.5 % ($Z \geq 11$). Due to large statistical error and very narrow energy range, it is very hard to conclude any dependence of projectile fragments production on kinetic energy of projectile from Fig. 5b.

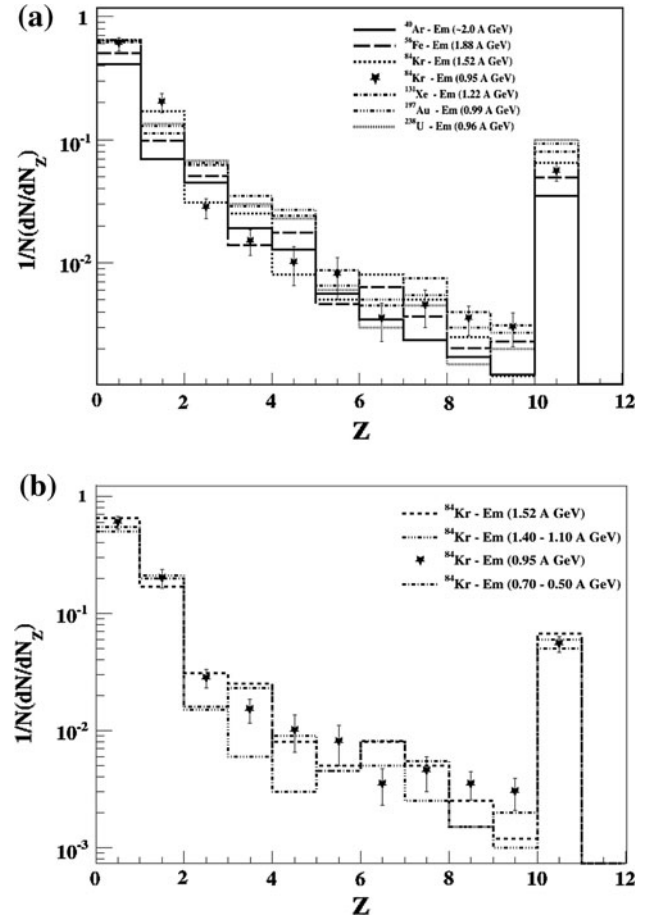


Fig. 5 Normalized estimated charge spectrum of different projectile at similar energy (a) and same projectile with different energy (b). ^{84}Kr at 0.95 [Present work] is compared with the results of ^{40}Ar at ~ 2 A GeV [16], ^{56}Fe at 1.88 A GeV [17–19], ^{84}Kr at 1.52 A GeV [20], ^{131}Xe at 1.22 A GeV [21], ^{197}Au at 0.99 [22], ^{238}U at 0.96 A GeV [23], ^{84}Kr at 1.40–1.10 [7], ^{84}Kr at 0.95 A GeV [Present work], ^{84}Kr at 0.70–0.50 A GeV [7]

3.2. Emission angle distribution of projectile fragment

The quantum mechanical features such as Fermi motion is considered to have influence on angular distribution of emitted particles. Therefore, it is interesting and also important to study and understand angular distribution of projectile fragments emitted in the interaction of $^{84}\text{Kr}_{36}$ with emulsion target at relativistic energy. The normalized projected angle distribution of identified single, double and multiple ($Z \geq 3$) charge projectile fragments emitted in interaction are shown in Fig. 6. The distributions are best fitted by the Gaussian function, $f(x) = p_0 \times \exp(-0.5 \times ((x-p_1)/p_2)^2)$.

The mean emission angle decreases with increase in charge of the projectile fragments is evident from Fig. 6. For single charge projectile fragments dispersion of distribution from the mean, 3.306 ± 0.125 , is largest and have value 3.260 ± 0.098 while sigma (mean) values of the

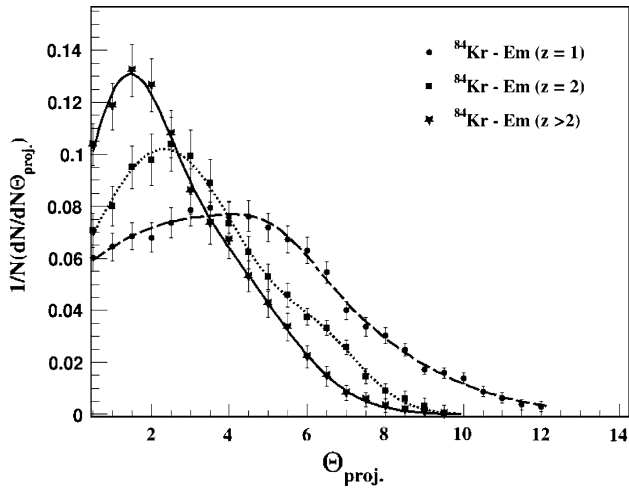


Fig. 6 The normalized distribution of projected angle for single, double and multiple charge PF's. The *points* represent experimental data and *solid, dotted and dashed lines* are the best fitting function line

fitted function are 2.564 ± 0.114 (2.268 ± 0.147) and 2.434 ± 0.119 (1.532 ± 0.182) for double and multiple charged projectile fragments, respectively. It also reflects that most (80 %) of the multiple charged fragments are emitted within 4° while for similar number of PF's emitting up to 5° and 7.5° for double and single charge PF's, respectively. It can be also seen from Fig. 6 that around 10.5, 7 and 6 % PF's having multiple, double and single charge, respectively are emitting at 0° .

The normalized dip angle distribution of PF tracks is shown in Fig. 7, fitted with above mentioned Gaussian function. From this figure, it is clear that the mean emission dip angle also decreases with increase in charge of PF's. For single charge projectile fragments dispersion of the distribution from the mean, 3.301 ± 0.138 , is largest and have value 3.409 ± 0.107 while sigma (mean) value of the fitted function are 2.723 ± 0.119 (2.344 ± 0.155) and 2.485 ± 0.135 (1.369 ± 0.209) for double and multiple charged projectile fragments, respectively. It also reflects that most of the multiple charged fragments are emitted within 4° while for similar number of PF's emitting up to 5° and 7° for double and single charge PF's, respectively. It can be also seen from Fig. 7 that around 11, 7.5 and 6 % PF's having multiple, double and single charge, respectively are emitting at 0° .

The normalized space angle distribution of projectile fragment tracks is shown in Fig. 8 fitted with above mentioned Gaussian function. From this figure, it can be seen that the mean emission space angle also shows similar trends as shown by projected and dip angle distributions, i.e. mean emission space angle decreases with increase in the charge of the projectile fragments. For single charge projectile fragments dispersion of the distribution from the

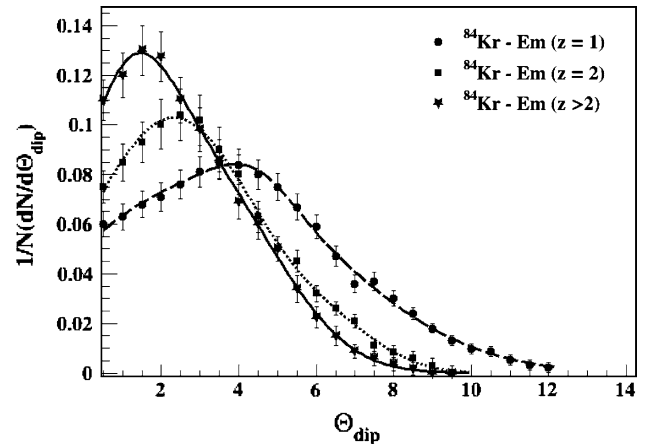


Fig. 7 The normalized distribution of dip angle for single, double and multiple charge PF's. The *points* are representing experimental data and *solid, dotted and dashed lines* are the best fitting function line

mean, 3.062 ± 0.115 , is largest and have value 2.676 ± 0.216 while sigma (mean) values of the fitted function are 2.515 ± 0.694 (2.303 ± 0.302) and 1.380 ± 0.409 (1.371 ± 0.159) for double and multiple charged projectile fragments, respectively. It also reflects that most of multiple charged fragments are emitted within 4° while for similar number of PF's emitting up to $\sim 6^\circ$ and $\sim 7^\circ$ for double and single charge PF's, respectively. It can be also seen from Fig. 8 that around 10.5, 7.5 and 5.5 % PF's having multiple, double and single charge, respectively are emitting at 0° .

For a given charged PF, the measured angle (projected, dip and space) depicts no significant change in the mean and sigma values. This is evident from Figs. 6, 7 and 8. Therefore, over all emission shapes for three major

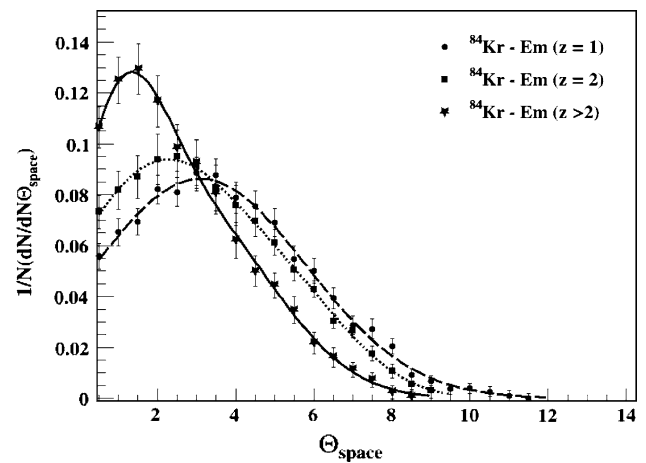


Fig. 8 The normalized distribution of space angle for single, double and multiple charge PF's. The *points* are representing experimental data and *solid, dotted and dashed lines* are the best fitting function line

projectile fragment groups is conical in shape in forward direction.

3.3. Emission angle distribution based on target species

The variation of emission angle (space angle) of fragments in ^{84}Kr interactions with individual target group [H, CNO, Ag(Br) and composite emulsion] for single, double and multiple charge PF's were studied and are depicted in Figs. 9, 10 and 11 respectively. The target identification and separation method for this experiment is explained in Ref. [4–7]. The experimental data points are represented by symbols and different types of lines (solid, dashed and dotted) are the best fitting function.

Figures 9, 10 and 11 represent normalized distribution of space angle for single, double and multiple charge projectile fragments emitted or decayed during interaction of $^{84}\text{Kr}_{36}$ beam with different emulsion detector target groups. 7, 9 and 9.5 % of PF's are emitted at zero angles for H-target, whereas for heaviest target group Ag(Br) 4, 5.5 and 10.5 % were observed for single, double and multiple charge projectile fragments, respectively. The maximum values of single charge PF's are 12, 10 and 8 %; for double charge PF's there are 11.5, 10 and 9 %; and for multiple charge PF's it is 10, 10.5 and 11 %, respectively for H, CNO, and Ag(Br) targets. Tailing portion of distribution also follows the similar pattern but in reverse order.

It can also be seen from Figs. 9, 10 and 11 for single, double and multiple PF's respectively that with the increase in mass number of target group the mean values of fitted function are shifting towards higher emission angle and the dispersion of distribution is also becoming wider. For a given type of PF's the shapes of all distributions are similar. These distributions are crossing each other in between 4° and 5° for single charge PF's, at $\sim 4^\circ$ of

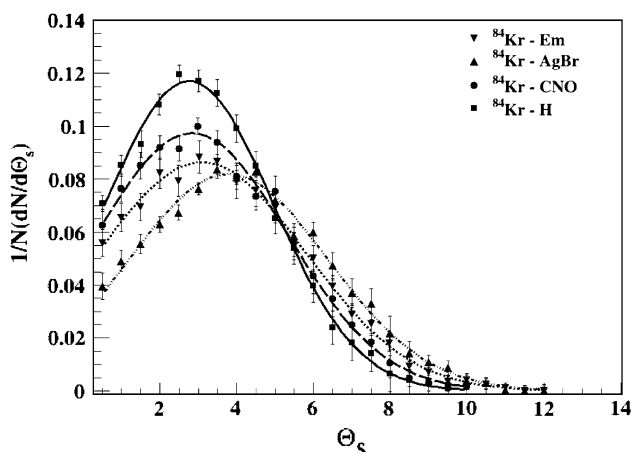


Fig. 9 The normalized distribution of space angle for single charge PF's. Points are representing experimental data and *solid, dotted and dashed lines* are the best fitting function line

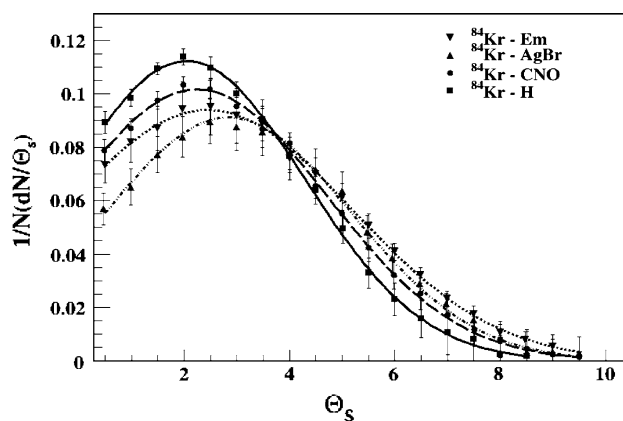


Fig. 10 The normalized distribution of space angle for double charge PF's. Points are the experimental data and *solid, dotted and dashed lines* are the best fitting function line

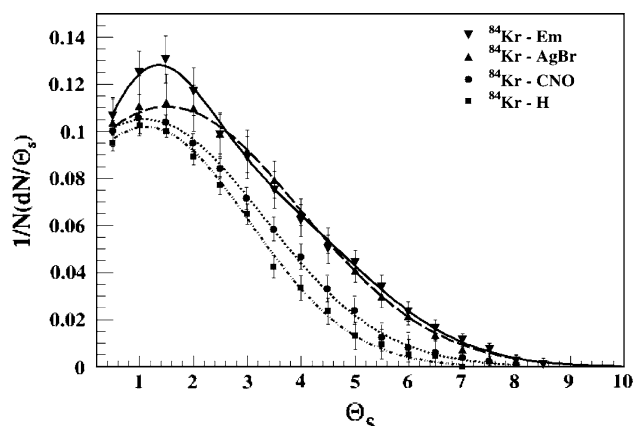


Fig. 11 The normalized distribution of space angle for multiple charge projectile fragments. Points are representing the experimental data and *solid, dotted and dashed lines* are the best fitting function

emission angle for double charge PF's and no one crosses each other in case of multiple charge PF's. This implies that, for single and double charge PF's at the above mentioned angles momentum transfer during interaction is almost similar for all the target species and after that number of PF's having larger momentum is large in case of heavier targets. Whereas for multiple charge PF's, momentum transfer during interactions is showing strong dependence on mass number of target group throughout the entire emission angles.

The distribution of fitted mean emission angle values are plotted with respect to charge of projectile fragments for different target groups including composite emulsion target is shown in Fig. 12. The figure infers a strong negative dependence of mean emission angle with respect to charge and positive dependence with mass number of target group. Therefore, the mean transverse momentum also follows similar dependent with charge of PF and mass number of

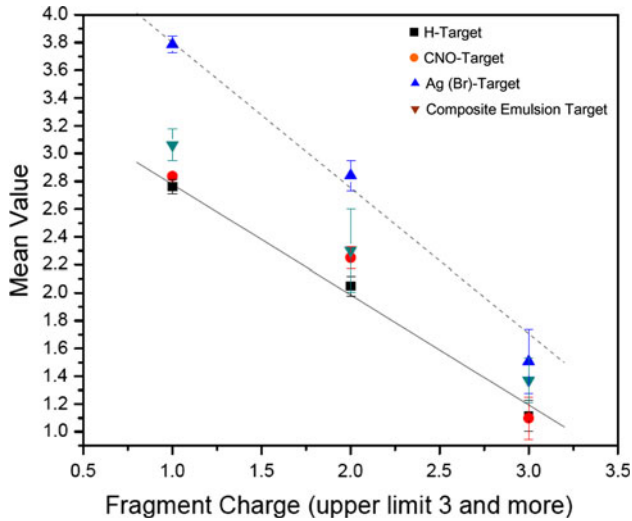


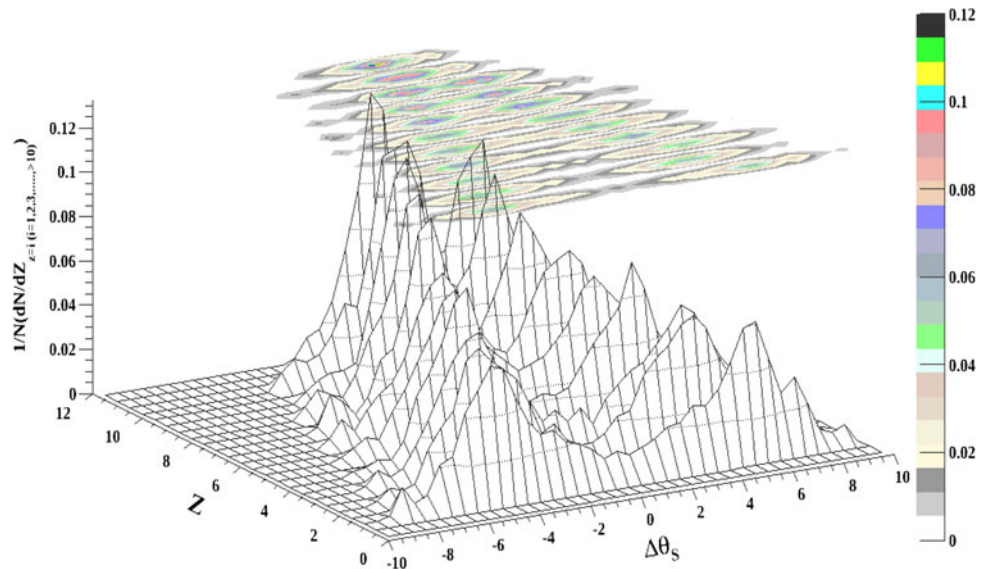
Fig. 12 Fitting function's mean value variation with charge of the projectile fragment for different emulsion target groups

target. This shows as the degree of breakup of target increases, i.e. the impact parameter decreases, a greater fraction of heavier projectile fragments, alphas and singly charged fragments scatters at larger angles within the forward cone because the transfer of momentum in general is larger in case of heavier mass number target.

3.4. Effects on emission angle due to the charge of associated projectile fragments

The details from above subsections make it interesting to study the effects on emission angle for different projectile fragments due to their associated projectile fragments. We have performed such study up to 10 charge unit of

Fig. 13 Normalized distribution of the space angle difference ($\Delta\theta_s$) of different charge projectile fragments with respect to the rest of the projectile fragments of the interactions



projectile fragments and clubbed the charges higher than 10 units together.

We have measured space angle difference ($\Delta\theta_s$) between considered projectile fragments with respect to the rest of the observed projectile fragments in an interaction and plotted normalized distribution of these difference with respect to charge of the projectile fragments in Fig. 13. Space angle difference is measured by considering PF of particular charge with respect to the rest projectile fragments of event referred to the charge of the considered PF. The positive and negative signs for angles are just representing upward and downward location of considered PF's with respect to the beam direction.

Lighter charge projectile fragments show larger dispersion from rest of projectile fragments as depicted in Fig. 13. It can be seen that lighter charge ($Z < 9$) projectile fragments show two peaks, one in positive (upward) and other one is in negative (downward) side. The heavier charge more than 10 charge units just merge and do not show two peaks behavior exhibited by lighter charge projectiles. The ratio of mean value of up and downward peaks distribution is shown in Fig. 14. We expect the peaks must be located at same position in upward and downward direction in the conical shape of forward cone, i.e. similar charge projectile fragments will emit at same angle. Such emission behaviour will reflect symmetrical nature and therefore the ratio of both side peaks position must be equal to 1. In Fig. 14, this ratio is shown by dotted line. The observed best fit distribution comes out to be 0.93 that is close to unity. Thus observations are close to the expected results. Therefore Fig. 3 proves symmetrical nature of projectile fragments emission. It may be concluded from Fig. 14 that the lighter charges show symmetry distribution behavior.

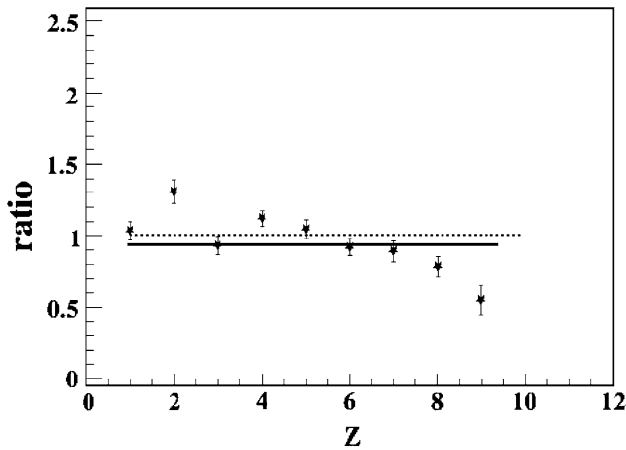


Fig. 14 The ratio of mean value of big peaks located *up* and *downward* of the *beam* direction is distributed

Figure 15 demonstrates that the ratio of the up to the downward peak area should be equal under certain fix value of sigma. Dotted line is the expected value of ratio and the solid line is the best fit of distribution is at 1.01 ± 0.04 . It may be concluded from Fig. 15, that almost equal number of projectile fragments for each charge are symmetrically emitted in interactions.

In Fig. 13, on careful examination one can see a small and distinctive peak on both sides of the later peaks. The ratio of mean and area of these small peaks are plotted in Figs. 15 and 16, respectively for symmetrical distribution. We have fitted the data point with best fitting function and found the mean value of each peak. From Fig. 16 it can be seen that the best fit line is slightly above (1.02) the expected line at one. It shows that the both small peaks have similar mean value, i.e. they are located at the same position but in opposite sides of the beam direction. It also shows that there are certain numbers of projectile fragment

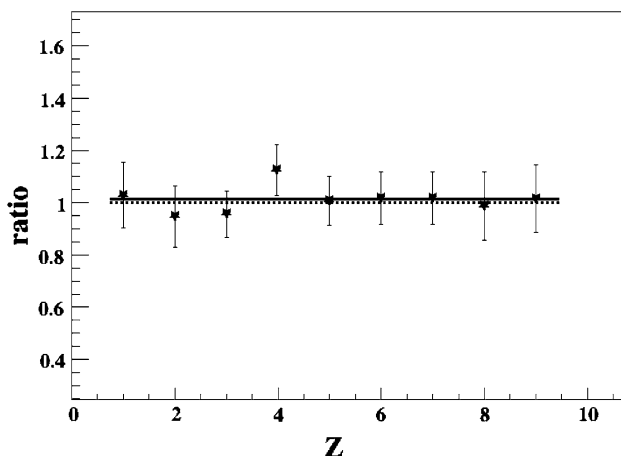


Fig. 15 Ratio of the area located under three sigma region of the big peaks located *up* and *downward* of the *beam* direction is distributed

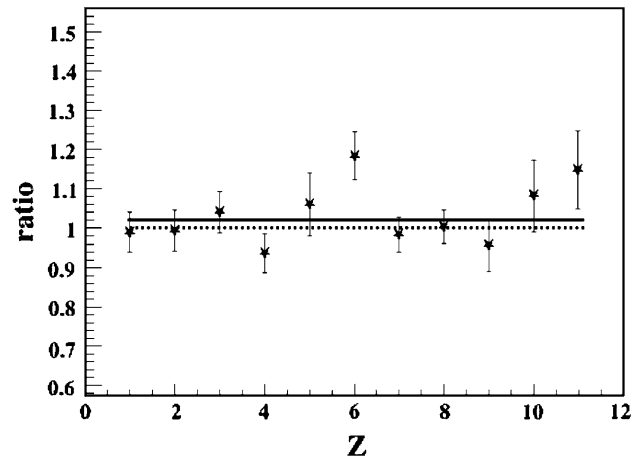


Fig. 16 Data point are the ratio of the mean values of small peak and *solid line* is the best fitting for data *point*, *dotted line* are expected value

of same charge having different emission value difference. It means some projectile fragments have different emission time and therefore it is possible that they are coming from the decay products of the heavier projectile fragments of the interactions.

The ratio of area under small peaks is plotted in Fig. 17. The best fit solid line (0.93) is close to the expected dotted line, showing similar area of the small peaks of all lighter charge within 7 % of the dispersion margin from the expected value. Here, we may assume that the similar small peaks are present at other side of the big peaks considering equal distribution. It means there are total four small peaks for each big peak for every lighter charge projectile fragments. On the basis of Fig. 17, we can consider almost equal area of those four peaks with 7 % dispersion margin. From Fig. 13, we can calculate that 14.30, 6.67, 8.75, 6.52, 9.12, 10.44, 15.80, 11.05 and 11.14 % of charge (Z) equal

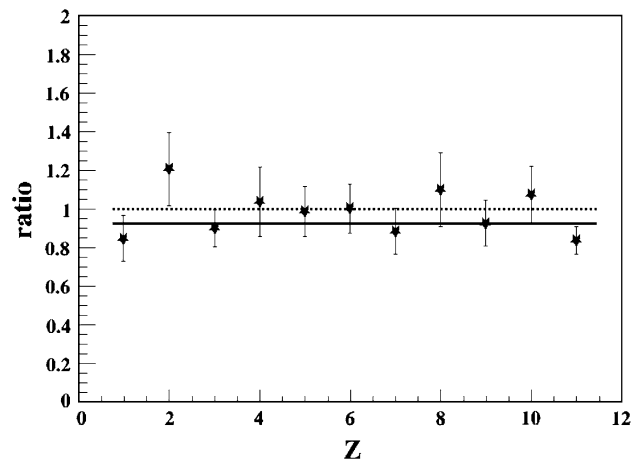


Fig. 17 Data points are the ratio of the area under small peak and *solid line* is the best fitting for data *point*, *dotted line* are expected value

to 1, 2, 3, 4, 5, 6, 7, 8 and 9, respectively of projectile fragments are not coming from direct interaction, i.e. are possibly coming from the decay process of heavy projectile fragments that are by products of direct interaction or may be some other process.

4. Conclusions

It is quite interesting to study the projectile fragmentation process of heavy ions such as ^{84}Kr projectile. The main conclusions of our experiment are as following.

In the above sections a detailed explanation were given on charge estimation of projectile fragment and angle measurements. From the study, we conclude that the production of heavy and intermediate mass fragments is a function of size of fragmenting system as well as the beam energy. Lighter charge and intermediate plus heavy charge projectile fragments such as $Z = 1$ and 2 and >10 show strong dependence on mass number of projectiles of similar energies. As charge of the projectile fragments increases their emission chances at zero degree also increases, i.e. there are less chance of emission at zero degree of single charge projectile fragment. But, lighter charge projectile fragments gaining more transverse momentum than heavier charge one. Our study shows emission distribution of projectile fragments and their transverse momentum has strong dependence on the target mass number.

The angle distribution study of projectile fragments reveals nature of fragments and the behavior of fragments on each other during emission that affects the Fermi's motion of the particle. From this study we observed the emitted projectile fragments are strongly affected by rest of the associated projectile fragments. The distribution of projectile fragments is showing symmetrical nature for lighter charge projectile fragments and as we move from lower to higher charge symmetrical distribution behavior decrease and both peak merge into a single peak. Therefore, heavy charge projectile fragments moving with nearly same velocity as the incident projectile, with very small

deviation in comparison to lighter charge projectile fragment and they are not affected too much by their neighbor projectile fragments. We also observed a small but significant amplitude peaks on both side of the big peak for almost all light charge projectile fragments having different $\Delta\theta$ values. It reflects, there are few percent of projectile fragments that are coming from the decay of heavy projectile fragments or any other process.

Acknowledgments Authors are grateful to the staff of the GSI, Germany for exposing the emulsion detector plates.

References

- [1] M Guler et al., CERN/SPSC 2000-028, SPSC/P318 (2000)
- [2] K Kodama et al., CERN/SPSC 99-20, SPSC/M635, LNGS-LOI 19/99 (1999)
- [3] D Ghosh et al., *IL Nuovo Cimento A* **105** 12 (1992)
- [4] M K Singh, R Pathak and V Singh *Indian J. Phys.* **84** 1257 (2010)
- [5] S L Goyal and N Kishore *Indian J. Phys.* **84** 553 (2010)
- [6] M K Singh, A K Soma, R Pathak and V Singh *Indian J. Phys.* **85** 1523 (2011)
- [7] N Hothi and S Bisht *Indian J. Phys.* **85** 1833 (2011)
- [8] S A Krasnov et al., *Czech. J. Phys.* **46** 531 (1996)
- [9] M K Singh, R Pathak and V Singh *J. Purv. Acad. Scie. (Phys. Scie.)* **18** 233 (2010)
- [10] H Bethe and J Ashkin *Experimental Nuclear Physics* (eds.) E Segré (New York: Wiley) p 253 (1953)
- [11] V Singh *PhD Thesis* (Banaras Hindu University, Varanasi) (1998)
- [12] V Singh et al., arXiv:nucl-ex/0412049v1 (2004)
- [13] R Bhanja et al., *Phys. Rev. Lett.* **54** 771 (1985)
- [14] P H Fowler et al., Blatt, University of Sydney, Mimeographed Report (1954)
- [15] P H Fowler et al., *Phil. Mag.* **46** 587 (1955)
- [16] C F Powell et al., (London: Pergamon) (1959).
- [17] S A Kalinin et al., *Russ. J. Sci. Ind.* **12** 29 (2000)
- [18] P Demers (Montreal: Univ. Montreal Press) (1958)
- [19] B Rossi *High Energy Particle* (New York: Prentice Hall inc.) **24** (1952)
- [20] D A Tidmen et al., *Proc. Roy. Soc. A.* **66** 1019 (1953)
- [21] P L Jain et al., *Phys. Rev. C.* **47**, 342 (1993)
- [22] C J Waddington et al., *Phys. Rev. C.* **31**, 888 (1985)
- [23] P L Jain et al., *Phys. Rev. Lett.* **68**, 1656 (1992)